A forward model for earthquake generation on interacting faults including tectonics, fluids, and stress transfer

Delphine D. Fitzenz and Stephen A. Miller

Department of Earth Sciences, Swiss Federal Institute of Technology, Zürich, Switzerland

Abstract. We present a forward model of interacting faults for systems of any geometry. The model generalizes that of *Miller et al.* [1996,1999] to a fully three-dimensional model where faults of any strike and geometry interact through an elastic matrix using the general solutions of *Okada* [1992]. The model includes large-scale plate motion loading and increasing pore pressures from a source term, undrained poroelastic effects, large coseismic hydraulic property changes, and porosity creation through dilatant slip. To illustrate the basic behavior and utility of the model, results are presented of the long-term evolution (≈ 9300 years) for a generic case of a blind, dipping fault and a subvertical strike-slip fault in a transpressional environment. We show the stress state evolution along both faults, seismicity time lines, quasi-static rupture propagation including rake angle changes, local and regional stress buildup and rotations, static and dynamic fault interactions, and ΔCFS (changes in Coulomb Failure Stress) within the fault system. Large compartments of varying overpressure result on both faults from coseismic pore pressure changes and contribute to the complexity of the stress state. For the considered case, we find that the poroelastic effects on the receiver fault are about twice the change in the shear stress, providing a significant contribution to the ΔCFS. Regional stress rotations in response to the model seismicity indicate that further model developments must include dynamic generation of new faults in response to the evolving tectonic regime.

1. Introduction

The long-term behavior of complex fault systems is poorly understood because the community lacks a forward model that includes the dominant physics of the earthquake process. Current models of stress transfer [*Stein et al.*, 1997; *Perfettini et al.*, 1999; *Harris and Day*, 1999; *Gomberg et al.*, 2000], although useful, are limited because the slip history and an a priori apparent friction coefficient (accounting for pore pressure) must be prescribed upon a fault system to calculate stress transfer to other faults. This limitation precludes forward modeling of the long-term evolution of faults. Mechanistic and quantitative seismic hazard assessment requires an understanding of faults and fault interaction, but the paucity of paleoseismic data [*Pantosti et al.*, 1993; *Meghraoui et al.*, 2000] and the short duration of the instrumented seismology (about one century) limit the seismicity catalogs needed to describe the system.

In the recent decades, earthquake research focused on a number of approaches using a variety of data to understand the earthquake process. These include studies of the origin of seismic complexity [*Bak and Tang*, 1989; *Ben-Zion and Rice*, 1993; *Rice*, 1993; *Miller et al.*, 1999] and theoretical and experimental developments on the physical processes involved in faulting, for example, friction [*Dieterich*, 1979; *Blanpied et al.*, 1998; *Scholz*, 1998; *Marone*, 1998], rupture initiation [*Dascalu et al.*, 2000; *Voisin et al.*, 2000], and the importance of the fault geometry [*Lockner and Byerlee*, 1993]. Numerous numerical earthquake models (see the review by *Robinson and Benites*, 1995) focus on different aspects of the earthquake process. These include stable versus unstable sliding [*Segall and Rice*, 1995], the effect of fluid migration [*Yamashita*, 1998] or pore creation due to slip on the seismicity [*Yamashita*, 1999], shear-enhanced compaction [*Sleep and Blanpied*, 1992; *Sleep and Blanpied*, 1994], and models of fault behavior [*Ben-Zion and Rice*, 1993; *Robinson and Benites*, 1996; *Rundle*, 1988]. These models are not three-dimensional, not fully forward (the first rupture is imposed), do not consider the interaction between stress and pore pressure [*Hardebeck and Hauksson*, 1999] or do not consider the "fault valve" aspect of fluid flow

(which requires that permeability be treated as a dynamical property within fault zones).

Fluids are widely believed to play an important role in earthquakes and faulting, and a number of studies focused on mechanisms for generating and maintaining high pore pressures within fault zones. Overpressures can result from frictional heating [Spray, 1995], creep compaction [King et al., 1994; Streit and Cox, 2000; Sleep and Blanpied, 1992; Sleep, 1995], dehydration of hydrous minerals, or a direct fluid source from a ductile root [Rice, 1992]. Conceptual models that identify the role of fluids include isolated compartments [Byerlee, 1993], and the fault valve model that recognizes the dynamical aspect of fluid flow and tectonic loading [Sibson, 1993; Miller et al., 1996].

Each of these studies provide important insight into certain aspects of the earthquake process, but a model that combines these components into a forward and deterministic model has not been developed. The purpose of this paper is to synthesize some of these components into a general and forward model that includes the dominant processes believed to control earthquakes and to investigate the faulting properties and the evolution of complex fault systems. The approach is to model processes occurring at the small scale and to allow these processes to evolve and find their equilibrium state in the large-scale system within which they operate.

The two dominant mechanical processes that we consider are the state of stress in the system, and the pressure of the fluids. The model generalizes that of Miller et al. [1996, 1999, submitted manuscript, 2000], which was limited to vertical strike-slip faults, to consider fault systems of any geometry. The primary mechanics that we consider at this stage are elastic dislocation theory, undrained poroelasticity, large coseismic permeability changes within the fault zone, and a simple switch from static to dynamic friction.

We assume that elastic dislocation theory is a good approximation for brittle crustal faulting as evidenced by the successes in modeling coseismic deformation from satellite interferometry [Massonnet et al., 1993] and stress-triggering models [Stein et al., 1997]. We further assume that pore pressures play an important role in the process [Hubbert and Rubey, 1959; Sibson, 1973; Rudnicki, 1985; Sibson, 1992] in that knowing (or modeling) both the state of stress and the state of pore fluid pressure on a fault is necessary to understand earthquake mechanics in intraplate and interplate regions. Observations of rock samples taken in fault zones [Robert and Boullier, 1993; Chester et al., 1993] substantiate the important role of fluids. Fluid-assisted processes are shown to be significant in the highly strained fault cores, evidenced by pervasive syntectonic alteration of the host rock minerals to zeolites and clays and by folded, sheared, and attenuated crosscutting veins of laumonites, albites, quartz, and calcite [Chester et al., 1993]. We also assume that mature fault zones are low-permeability, fluid-saturated zones that coseismically change to high-permeability fracture zones (e.g., the fault valve model). Finally, we assume a rigorous quasi-static model, ignoring for now time-dependent processes of wave propagation and diffusion.

We explore model results from a generic blind dipping, strike-slip fault system to determine how this system evolves in time with stress interaction between the two faults. The model is adaptable to any fault system in any tectonic environment. Modifications and improvements to the models of Miller include, (1) monitoring the full stress tensor, (2) undrained poroelastic effects, (3) oblique loading from the base of the fault system, and (4) a separation of elastic stress transfer rupture propagation and pore pressure redistribution. We show (1) the stress state evolution and generation of pore pressure compartments, (2) seismicity time lines and frequency-size statistics, (3) slip and rake angle evolution during rupture, (4) slip distributions, (5) fault interaction during rupture, (6) principal stresses and orientation along a profile perpendicular to fault strike, and (7) ΔCFS (changes in Coulomb Failure Stress) due to a large event on the strike-slip fault and subsequent earthquakes on the strike-slip fault, on the dipping fault, and on optimally oriented faults. We consider the problem from a tectonic scale while keeping small-scale processes intact. We make significant approximations to simplify the physics, but we try to ensure that these approximations have substantial supporting evidence. We discuss the model assumptions in detail and the physical processes not currently considered. We also propose some directions for future research.

2. The Model

An arbitrary generic model that we chose to investigate is a coupled blind dipping-strike slip fault system (Figure 1) in a transpressional environment. The faults consist of a matrix of computational cells representing rectangular dislocations and discrete sealed fluid pressure compartments in a deforming elastic half-space. Central to our approach is coupling the analytical elastic deformation solutions of Okada [1985, 1992] to the coseismic permeability-change conceptual model of Miller et al. [1996]. The permeability of these compartments is taken as zero in the interseismic periods and very large (e.g., allowing for an "instantaneous" pore pressure redistribution; see Miller and Nur [2000], S. A. Miller (submitted manuscript, 2000), and equation (5)) when a rupture occurs. Plate motion is represented as a displacement through time on a dislocation plane located at the base of the seismogenic layer, infinite in all directions except along the plate boundary. Plate motion increases shear stress, normal stress, and pore pressure (through poroelasticity) along the fault planes, while pore pressures increase through poroelas-
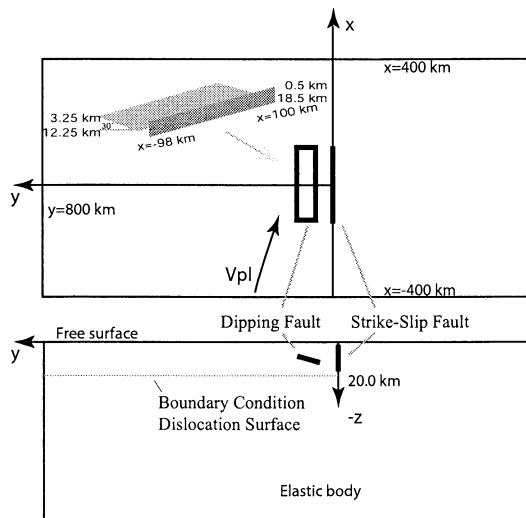
Figure 1. Model of a coupled blind-dipping, strike-slip fault system. The 3-D model is made of two faults discretized into computational cells, interacting through an elastic half-space, in a transpressional environment. Plate motion is imposed at the base of the seismogenic layer as a dislocation. The base is infinite in any direction, one edge being at the downward edge of the strike-slip fault.

tic effects and assumed pore closure within the faults. When a cell reaches the Coulomb failure stress, we use *Okada*'s [1985, 1992] analytical solutions to calculate the stress changes on all other cells of the faults. For a given dislocation vector applied on a rectangular plane at depth, these equations [*Okada*, 1992, Tables 6 to 9] provide the displacement vector and the displacement derivatives in any location in the surrounding elastic half-space (Poisson solid). From the strain tensor we calculate the stress tensor using Hooke's law and the resolved shear and normal stress along the prescribed fault planes. Slip is calculated through the stress drop at rupture. For a given cell we calculate the stress drop induced by a unit slip in the direction of the maximum shear stress, and we then invert the rate to obtain the slip magnitude that causes this stress drop [see also *Robinson and Benites*, 1995]. Note that this assumption relates only to the stress drop per subevent and not to the total (static) stress drop after a rupture (see Section 4). We include the following physical processes in this model: (1) quasi-static tectonic loading, (2) fluid-saturated faults, (3) fluid sources (either a direct fluid source or a pore space reduction mechanism), (4) elastic dislocation theory, (5) poroelasticity in undrained conditions, (6) small-scale coseismic changes in hydraulic properties, (7) porosity creation due to slip [*Sleep*, 1995], and (8) a switch from static to dynamic friction when a cell starts to slip (see discussion by Miller (submitted manuscript, 2000)). We monitor the full stress tensor and the static and coseismic fault interaction (throughout quasi-static rupture propagation). We assume heterogeneous fluid sources and

a displacement boundary condition at the base of the model fault system (e.g., all tectonic loading is applied via basal drag from the underlying ductile lithosphere).

2.1. Choice of Initial Conditions and Processes

2.1.1. Model geometry. The model geometry is imposed, and we focus here on the example of a coupled blind dipping/strike-slip fault system in a transpressional environment. Such coupled systems are observed in nature, with varying distance between the strike-slip fault and the thrust fault, for instance, near the big bend in central California (e.g., San Andreas/Kettleman Hills, [*Ekström et al.*, 1992]). The subvertical (dip of 85°) strike-slip fault acts as the plate boundary. The dipping fault is an intraplate fault dipping at 30°, buried from a depth of 3 km and extending to 12.25 km and parallel to the strike-slip fault. Both faults measure 200 km (from x=-100 to +100 km and $y > 0$) by 18.5 km (downdip), consisting of 3700 computational cells each. The minimum distance between the two faults is 10 km. The plate motion vector is dominantly subparallel but has a fault normal component (oriented 15° to the fault strike) and is applied uniformly on a horizontal plane lying at 20 km depth. The initial conditions are listed in Table 1. Shear stress is initially zero on the fault system at t=0, and the initial normal stress is assumed to be the lithostatic stress.

2.1.2. Pore pressure. It is generally accepted that the fractures are interconnected and the pore pressure gradient is hydrostatic at shallow depths, while excess pore pressures likely exist below ~3 km depth (see review by *Quattrocchi* [1999]). For computational convenience, we assume an initial uniform overpressure of $\lambda = P_f/\sigma_n = 0.7$ below 3 km depth for the strike-slip fault and a hydrostatic pressure gradient for the dipping fault. We impose a constant hydraulic head boundary condition on the first row of cells on each fault. Since the top of the strike-slip fault is near the surface (500 m), it implies that the pore pressure of all the regions of the fault temporarily connected to the first row becomes hydrostatic.

Pore pressures increase from a poroelastic effect approximated by

$$\Delta P_f|_{\text{no flow}} = B \times \frac{\text{tr}(\Delta\sigma)}{3}, \qquad (1)$$

where P_f is the pore pressure, $\text{tr}(\Delta\sigma)$ is the trace of the tensor of stress changes (positive in compression), and B is Skempton's coefficient. Equation (1) is applied in undrained conditions (no flow) on sealed compartments of homogeneous pore pressure. B is a nondimensional parameter of poroelasticity related to the contrast between the compressibility of the fluids and the compressibility of the rock: $B = (K_u - K)/(\alpha \times K_u)$, where K_u is the effective modulus of a porous medium filled by a fluid of compressibility β_f, K is the effective modulus of a porous rock saturated by a fluid at

Table 1. Model Parameters and Initial Conditions

Initial Model Parameters	Range of Values
Cell size	2000 m along strike by 500 m updip
Fault area	200 km along strike by 18.5 km updip
Plate velocity	35 mm yr^{-1} oriented 15° to the fault strike
Lame coefficients	$\lambda_{\text{lame}} = G = 30x10^9$ Pa,
Time step	time required to initiate failure on exactly one cell
Compressibility $\beta = \beta_\phi + \beta_f$	10^{-3} MPa^{-1}
Porosity ϕ	initial, 5%; maximum, 9%
Skempton coefficient B	0.6
Initial normal stress	lithostatic, $\rho_r gz$, $\rho_r = 2700$ kg m^{-3}
Initial shear stress	0
Initial pore pressure gradient	hydrostatic except for $-z > 3$ km depth on the strike-slip fault: 0.7* normal stress
Compaction	for $-z < 3$ km, $\dot\phi = 0$ for $-z > 3$ km, $0.8x10^{-6} < \dot\phi < 0.5x10^{-5}$ year^{-1}
Fluid sources $\dot\Gamma$	none
Friction coefficients	static, $\mu_s = 0.6$; dynamic, $\mu_d = 0.5$
Dilatation coefficient[a] β_m/W	18x10^3

[a]After *Sleep* [1995]

constant pressure P_f (dependent only on the compressibility of the solid phase and porosity), and α is the coefficient in the law of effective stress ($\sigma_{\text{eff}} = \sigma_n - \alpha P_f$, $\alpha \sim 1$ [*Nur and Byerlee*, 1971]). Generally, $K_u > K$, since it is more difficult to deform a rock when fluids cannot flow. For a very porous medium (K small), B tends toward 1, and for a very compressible fluid ($K \sim K_u$), B tends toward 0. As pointed out by *Scholz* [1990], the geometry is also very important. *Scholz* [1990, p. 329] writes that for a change in uniaxial stress in a cracked solid where the cracks are perpendicular to the stress, B is ~ 1, whereas for parallel cracks, B is almost 0. Using the undrained response of the Bad Creek Reservoir (South Carolina), *Talwani et al.* [1999] determined an in situ estimate value 0.66 for the Skempton's coefficient of a shallow shear zone in a gneiss massif. In their review of experimental observations, *Beeler et al.* [2000] report the range for B as 0.5-0.9 for granites, sandstones, and marbles. In this simulation, having no constraint on this parameter, we chose a value of 0.6.

Pore pressure can also change in the sealed compartments by reducing the available pore space, or by a direct "fluid pressure source" via

$$\frac{\partial P_f}{\partial t}\Big|_{\text{no flow}} = \frac{\dot\Gamma - \dot\phi}{\phi(\beta_\phi + \beta_f)}, \qquad (2)$$

where ϕ is the porosity, β_ϕ and β_f are the pore and fluid compressibility, $-\dot\phi$ is a rate of inelastic porosity reduction (e.g., from pressure solution, compaction) and $\dot\Gamma$ is a direct fluid source. Fluid sources are necessary to maintain overpressures because in the absence of a mechanism to increase pore pressure, diffusion would reduce pore pressures to hydrostatic over long timescales. In fault zones, substantial evidence suggests that pore

pressures are in excess of hydrostatic, implying that a fluid source must exist [*Quattrocchi*, 1999; *Byerlee*, 1993]. Many different mechanisms are possible for the fluid sources, most of which are unconstrained. Potential fluid sources include, among others, creep compaction [*Sleep and Blanpied*, 1994] and dehydration of hydrous minerals (namely, through frictional heating [*Spray*, 1995; *Rice and Cleary*, 1976]). No detailed mechanism for fault zone compaction or fault creep is explicitly considered. One such mechanism was proposed by *Sleep and Blanpied* [1994], who constructed a model (based on experimental observations) in which compaction is due to ductile shear creep between seismic events in the earthquake cycle. Such grain-scale creep results from deformation at grain-grain contact points due to deformation under stresses. The deformation process can be cracking, dissolution, crystal plasticity, etc. This mechanism is very efficient at elevating pore pressure even for very small amount of creep and is a viable mechanism for increasing pore pressure in fault zones. As in the present work, they assumed that fluids cannot escape the fault zone. Another compaction mechanism could be the mechanical compaction (rearrangement of grains) due to increased normal stress. This would require that grains be able to slide past each other, and conditions in which this would be possible (values of normal stress, initial porosity, grain size, friction) are to be investigated. Since fluid sources are unconstrained, we assume a random distribution (over a small range) of sources, either via a direct fluid source $\dot\Gamma$ or a plastic pore closure $\dot\phi$ (only $\dot\phi$ is considered in the present study). Although we recognize their importance, we do not include any depth or temperature dependence at this point. Any or all of the terms in (1) or (2) can be randomized, and any one of these

would provide an initial heterogeneity. Without this heterogeneity the faults would initially break row by row, since the boundary conditions (size of the plate) are chosen to avoid lateral changes in the effect of tectonic loading. Other properties could also be arguably randomized (i.e., fault zone width or porosity) but are made uniform in this model. No other assumptions are imposed as initial conditions (e.g., overpressured patch, initial hypocenter).

2.1.3. Coulomb failure. The failure stress is the Coulomb failure stress that explicitly includes the pore pressure state. The initial static friction coefficient (μ_s) is taken constant and uniform over the fault planes and is assumed to be 0.6. When slip occurs, friction reduces to a dynamic value $(\mu_d = 0.5)$ for the duration of that event. This switch approximates a slip-weakening model for friction and is discussed by Miller (submitted manuscript, 2000). After the event, friction is reset to the static value. An important aspect of friction that we currently ignore is the increase in friction with time between two plates in stationary contact (e.g., a fault zone): $\mu \propto \log(t)$. This logarithmic time dependence has a physical basis in terms of yielding between points of contact [*Scholz*, 1990, pp.46-80] and is widely supported by experimental observations. We recognize the importance of this strengthening but do not include it here because it adds another level of iteration when determining the time step necessary to initiate one hypocenter (e.g., rigorously quasi-static). Incorporating a full rate-and-state constitutive friction law (see *Dieterich* [1979], and review by *Gomberg et al.* [2000]) is beyond the scope of the current study.

Ruptures propagate along the predefined fault planes, although *Kame and Yamashita* [1999] show that rapidly growing cracks have a natural tendency to spontaneously curve and have a large impact on the arresting mechanism of earthquake ruptures. Other evidence shows that a rupture can stop on a nonfavorably oriented preexisting fault and propagate farther by creating new optimally oriented cracks in the country rock (e.g., the Landers earthquake [*Bouchon et al.*, 1998a]). In future model developments, the constraint of rupture along predefined planes will be lifted by generating new failure planes in response to the stress state of the system.

2.1.4. Dilatant slip. Porosity production is modeled by frictional dilatancy and is assumed to be proportional to slip. In fault zone dilatancy models (see review by *Scholz* [1990]), dilatancy is assumed to occur within the fault zone as slip occurs during nucleation (due to joint dilatancy) in which the fault walls must move apart to accommodate slip (interlocking, ridingup) or due to shear of granular material (breccia, gouge) within the fault zone. Porosity production follows the model of *Sleep* [1995]:

$$\frac{\partial \phi}{\partial \delta} = \frac{\beta_m(\phi_m - \phi)\tau}{W\phi_m\sigma_n}, \qquad (3)$$

where ϕ is the porosity created with slip δ, β_m is the

fraction of energy that goes into the new crack creation, ϕ_m is the saturation porosity which limits the amount of crack porosity that can be generated, τ and σ_n are the shear and normal stress acting on the slipped cell, and W is the fault zone width. The values for β_m, ϕ_m, and W were taken from *Sleep* [1995]. The porosity change is used to update the storage capacity $(\beta_\phi\phi)$ of the cells just before the redistribution of pore pressure. Because porosity changes through dilatant slip, the rate at which pore pressures increase (equation (2)) for any cell also changes in time due to the porosity dependence of the pore pressure increase rate.

2.2. The numerical model

The flowchart of the model algorithm is shown in Figure 2. After setting the initial conditions the time step necessary to initiate failure of exactly one cell is calcu-
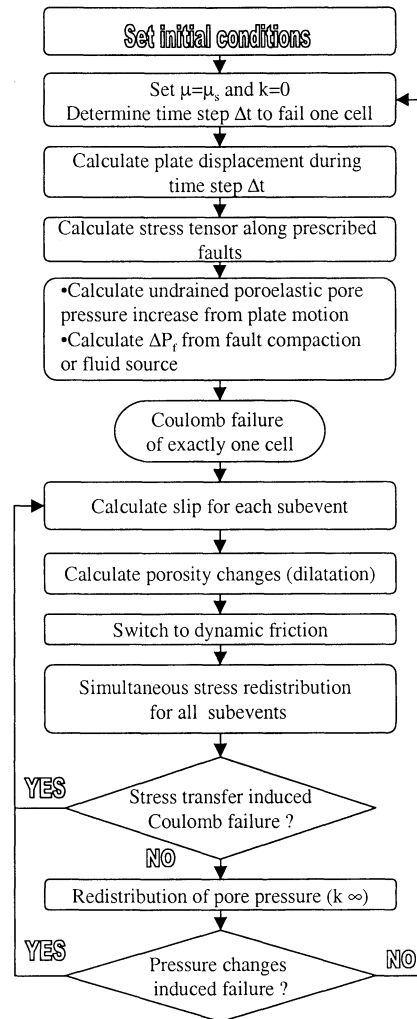

Figure 2. Flowchart of model algorithm. The model includes quasi-static tectonic loading, fluid-saturated faults, fluid sources, elastic dislocation theory, poroelasticity in undrained conditions, small-scale coseismic changes in hydraulic properties, frictional dilatation, and monitoring of full stress tensor. (See text for more details.)

lated by solving (4) for each cell i and by choosing the minimum of the calculated time steps Δt_i. Δt_i is the exact time step needed to bring cell i (which stress state is known at time t) to brittle failure:

$$\Delta t_i = -\frac{\mu_s \times [(\sigma_n)_i + (P_f)_i] + \tau_i}{\Delta \tau_i + \mu_s \times [(\Delta \sigma_n)_i + (\Delta P_f)_i]}, \qquad (4)$$

where $(\Delta \sigma_n)_i$, $\Delta \tau_i$, and $(\Delta P_f)_i$ are increments of normal stress, shear stress, and pore pressure per time unit, respectively. $(\Delta P_f)_i$ includes both the poroelastic changes (equation (1)) and the effect of the source term (equation (2)) . The plate displacement is then calculated for this time interval, and the stresses and pore pressures are calculated for all cells of the fault system. For the cell that reached the Coulomb failure condition we calculate the amount of slip needed to decrease the shear stress by the assumed stress drop (25% of the prefailure stress in the simulation studied below, see discussion in section 3.3). The porosity created through this dilatant slip event is calculated with equation (3) [Sleep, 1995], the friction coefficient of the cell that failed is reduced to the dynamic friction value, and the cell hydraulically communicates with its nearest neighbors. The new stress state is then calculated on both faults. The changes in stresses and pore pressure from the failure of this cell (still in undrained conditions) can initiate failure of other cells, and the model is then cycled until all cells are below the failure condition.

Assuming that propagation of the rupture front is much faster than fluid flow, the elastic and undrained poroelastic stress changes equilibrate before pore pressures are equilibrated. This scenario is presumably more realistic than the model of Miller et al. [1999], who redistributed pore pressure simultaneously with the stress transfer.

Pore pressure redistribution among cells that failed is calculated by conserving fluid mass [Miller et al., 1999]:

$$\bar{P}_f = \frac{\sum_{i=1}^{m} (\phi \beta)_i (P_{f_i} - \rho g \Delta z)}{\sum_{i=1}^{m} (\phi \beta)_i} + \rho g \Delta z, \qquad (5)$$

where ρ is the fluid density, $\bar{P}_f$ is the equilibrium fluid pressure among the m affected cells, weighted by the storage capacity of each cell $(\phi \beta)_i$, and appended with a hydrostatic gradient with depth. The term Δz is measured from the depth of the slipped source cell, so a negative sign accompanies the shallower cells.

Pore pressure redistribution may induce additional failures, and if so, the algorithm returns to the "undrained rupture" loop just described. This sequence is then cycled until the system is in equilibrium. These (quasi-static) rupture loops ignore wave propagation but provide insight into the propagation of the ruptures and coseismic stress transfers. Before the next time step is calculated, permeability is reinitialized to zero (all cells are sealed) and the friction coefficient is reset to the static value. The redistribution of the stresses is made simultaneously in the case of multiple failures during the same sequence in the same time step.

3. Model Results

3.1. Seismicity Time Line and Frequency-Magnitude Statistics

The seismicity time lines are shown for the strike-slip fault and for the dipping fault in Figure 3. The minimum moment magnitude (M_w) is ~3.8 because of the size of the subfaults (or cells, i.e., 2 km along strike by 0.5 km along dip). M_w is calculated from the scalar seismic moment via
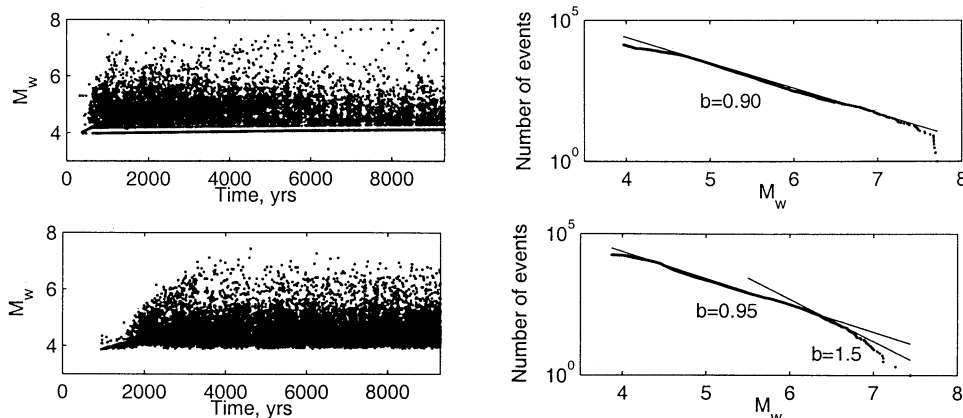

Figure 3. (left) Seismicity time line and (right) corresponding frequency-magnitude relationship for (top) the strike-slip fault and (bottom) the dipping fault. The minimum moment magnitude (M_w) is ~3.8 because of the size of the subfaults (or cells, i.e., 2 km along strike by 0.5 km along dip). M_w is calculated from the scalar seismic moment via equation (5). The maximum moment magnitude for the time window (~ 9300 years) studied is $M_w \sim 7.7$. The frequency-size statistics show that a wide range of event size are generated in this model with b-values ~ 1 for each fault.

$$M_w = \frac{2}{3}\log_{10} M_O - 10.7, \qquad (6)$$

where M_O (in dyn cm) is measured in the model. For example, 10 cm of slip on one cell corresponds to a moment magnitude of $M_w = 3.62$. The maximum moment magnitude for the time window ($\approx$ 9300 years) studied is $M_w \sim 7.7$ representing failing of a patch on the order of 18 km in depth by 100 km.

Seismicity first appears on the plate boundary strike-slip fault because of a higher stress buildup rate. The boundary (see Figure 1) between the moving elastic layer ($y > 0$ and $z > -20$ km) dragged from the base and its elastic symmetric counterpart ($y < 0$ and $z > -20$ km), free of imposed motion and welded on top of the elastic half-space defined by $z < -20$ km, undergoes large stress concentrations that increase with depth. This affects mostly the strike-slip fault since the dipping fault is both shallower and farther from the plate boundary. Therefore no rupture occurs on the "intraplate" dipping fault during the first 949 years, during which high pore pressures are being builtup. Once the effective stress is low enough (e.g., high pore pressures), the failure criterion can be reached even for low shear stresses, and the seismicity begins on the dipping fault (see also discussion below). The first large events ($M_w > 6.5$) occur after 990 years of loading on the strike-slip fault and after 3051 years on the dipping fault, about the time necessary to fail large portions of the initially unstressed fault.

The frequency-size statistics (Gutenberg-Richter (GR) empirical laws) show that a wide range of event size is generated in this model with b values of ~ 1 for each fault. This is consistent with other dislocation models that assume highly heterogeneous fault strengths [Robinson and Benites, 1995; Ben-Zion and Rice, 1995]. The GR laws also exhibit a change in the slope to 1.5 about $M_w > 6.5$, consistent with theoretical predictions

[Rundle, 1989]. This change is related to a change in the dimensionality where small earthquakes can grow in both length and width (two dimensions), while large earthquakes have no bounds in rupture length but their downdip width is limited by the thickness of the seismogenic layer [Pacheco et al., 1992]. In this model, heterogeneous fault strengths naturally arise through the complex stress paths followed in the $\tau - \sigma_{\mathrm{eff}}$ stress state.

3.2. Fault Stress State Evolution

Figure 4 shows the evolution of the stress state on the strike-slip fault and on the dipping fault (see Table 1). The stress state on both faults becomes complex because of the dynamical interaction between changes in stress and pore pressure. That is, when a large rupture occurs, dramatic pore pressure changes on the strike-slip fault lead to a compartmentalization of the fluid pressure distribution (see Figure 5a, left). These large compartments differ from the results of Miller et al. [1999] and are related both to the initial conditions in the first 3 km (hydrostatic pore pressure and no source term) and the manner in which pore pressure is redistributed. In the current model, pore pressures are redistributed only after stress transfer is equilibrated. For ruptures that propagate upward and laterally at shallow depths the final slipping patch includes numerous cells at hydrostatic pore pressure from the constant head boundary condition. Therefore, when pore pressure is redistributed, it can drop dramatically (e.g. from $\lambda > 0.8$ down to $\lambda \sim 0.5$, see Figure 5a, left). These large-scale pore pressure changes shift the corresponding points to the right in Mohr space (Figure 4). Conversely, the shear stress distribution does not develop such compartments (see Figure 5a, right). These zones of low pore pressure and shear stress subsequently act as "locked" parts of the fault because of the time needed
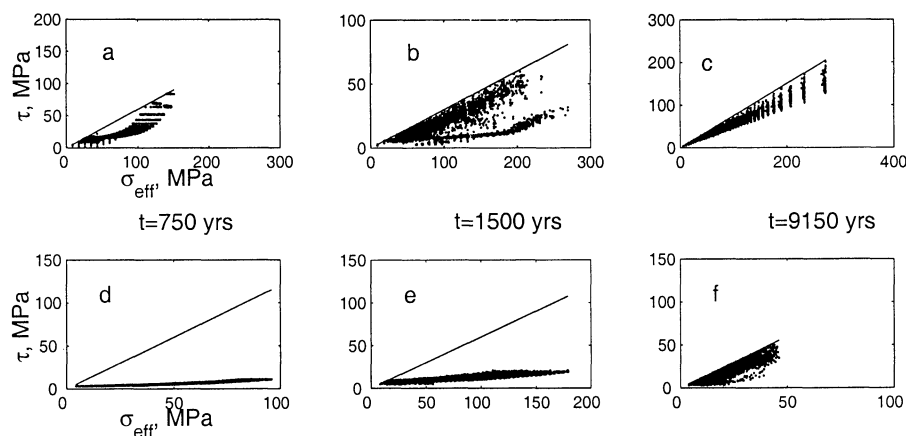

Figure 4. Time evolution of the stress state (a-c) on the strike-slip fault and (d-f) on the dipping fault. The dipping fault is highly overpressured (the range in σ_{eff} is small). The stress state tends to fill the space available between the static friction and the line defined by the stress drop until a large rupture occurs and relieves the fault by dramatically reducing pore pressure.
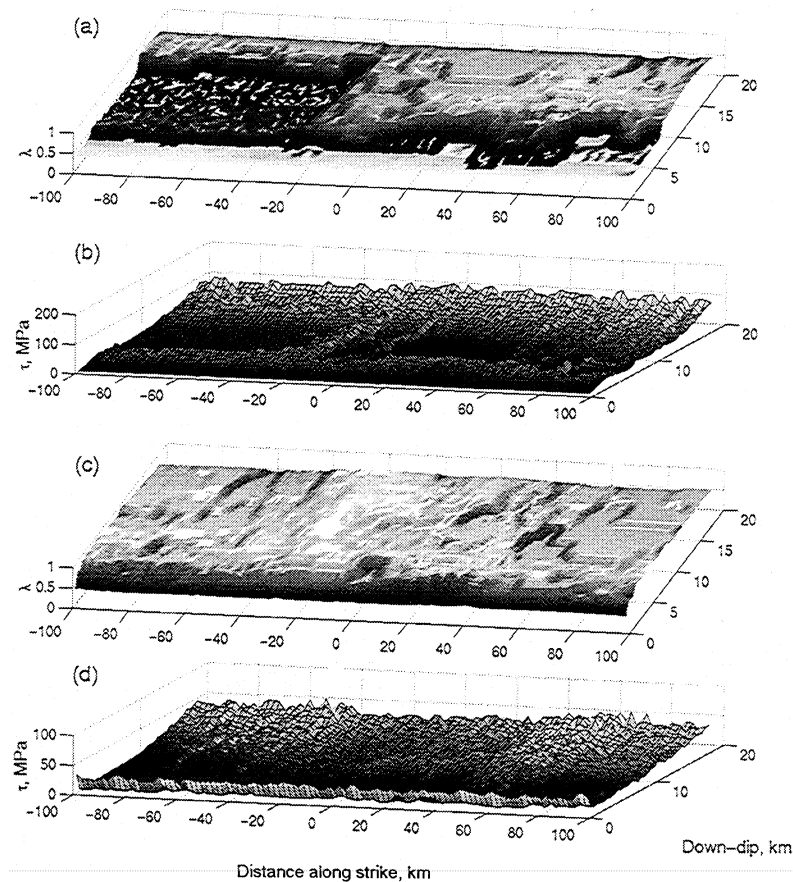
Figure 5.   (a) Pore pressure compartments on the strike-slip fault at t=1500 years. The vertical axis is $\lambda = P_f/\sigma_n$. Its values range from 0.4 (e.g., at the top of the fault, refering to a hydrostatic pore pressure gradient) to values close to 0.9 (highly overpressured compartments). We note that the heterogeneity imposed in the pore pressure increase rate acts as noise superposed on significant heterogeneities due to slip and subsequent pore space creation and pore pressure redistribution. (b) Shear stress distribution on the strike-slip fault at the same time. (c) Pore pressure compartments on the dipping fault at t=5400 years. (d) Corresponding shear stress distribution.

to rebuild pore pressure and/or shear stresses to the failure condition. Pore pressure compartments also develop on the dipping fault but with a smaller range of pore pressure (see Figures 5c-5d). On both faults, these compartments gradually increase in pressure with time from the assumed pore pressure increase rate and change abruptly when a rupture propagates within the fault system. Abrupt pore pressure change can occur through redistribution or due to the poroelastic effect. On the contrary, the stress state on the dipping fault is confined to a small region of stress space. High pore pressures limit the normal stress direction ($\lambda = P_f/\sigma_n$ in the range 0.70-0.95), and the shallow depth interval (from 3 to 12 km) limits the range of possible shear stress states. The difference in the behavior of the two faults is illustrated by the time evolution of their average shear stress, effective stress, and pore pressure (Figure 6). Each abrupt change in slope corresponds to a model earthquake. We notice the rather short onset of rupture on the strike-slip fault (bold lines) and how large events can reduce the mean shear stress but

also, and to a larger extent, the mean pore pressure. Stress builds slowly on the dipping fault and no earthquakes happen before the fault is highly overpressured. After 6000 years, both faults have reached a dynamic equilibrium (e.g., pseudo-steady state). The strike-slip fault, though initially overpressured, has evolved to a strong fault (approximately hydrostatic fluid pressures and high shear stress), whereas the dipping fault has become weak. This occurs because of the connection of the strike-slip fault to the hydrostatic surface, while the (buried) dipping fault increases in pore pressure during the slow buildup of shear stresses and never hydraulically communicates with the surface. Although this particular system evolved in this manner, it should not be generalized that all shallow dipping faults are overpressured.

3.3. Slip Vectors During Rupture

When the stress state on a fault has organized to a point where stress transfer and poroelastic effects can sustain a propagating rupture, slip on one cell can cas-
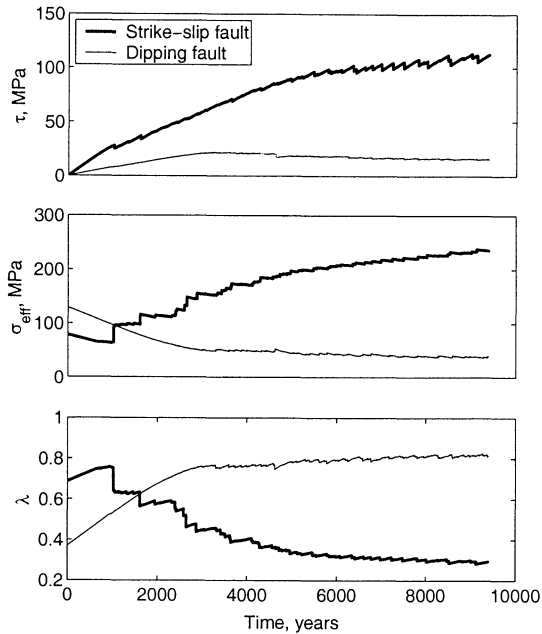
Figure 6. Average properties of the faults versus time. (top) Mean shear stress, (middle) Mean effective stress, (bottom) Mean pore pressure. Each abrupt change in slope corresponds to a model earthquake. We notice the rather short onset of rupture on the strike-slip fault (bold lines) and how large events can reduce the mean shear stress but also, and to a larger extent, the mean pore pressure. Stress builds slowly on the dipping fault, and no earthquakes happen before the fault is highly overpressured. After 6000 years, both faults have reached a dynamic equilibrium (pseudo-steady state).

cade through this stress state and generate large events. Here we investigate a $M_w = 7.20$ event spontaneously generated on the subvertical strike-slip fault at around 5500 years to illustrate some of the properties of these large events. We explore the propagation of slip, the evolution of the rake angle, and the stress interaction between the two faults. Figure 7 shows the quasi-static propagation of slip for one rupture. The gray scale shows the cumulative slip and the arrows show the slip vector (rake angle) during the event. The updip component is shown with a vertical exaggeration of 10 since the slip vectors on the strike-slip fault are predominantly strike slip. The rupture initiates, propagates upwards throughout the whole fault width, reaches the top of the fault (Figure 7a) and then starts propagating laterally (Figure 7b). The final slip and rake angle distribution is shown on Figure 7f. The final slip distribution of this event shows a heterogeneous slip distribution, with a maximum slip of 7.32 m. The maximum lateral extension of the rupture is 50 km, and the maximum width is the width of the fault plane (18 km). Though the rupture initiated at x=-82 km, coseismic stress transfer was enough to make the rupture front jump over 20 km (see Figure 7b) and propagate to 50 km along strike. We observe changes in the rake an-

gle during rupture propagation, a common seismological observation [e.g., *Bouchon et al.*, 1998b]. Changes in the rake angle have been investigated as a potential tool for initial stress determination from ground motion records inversion [*Spudich*, 1992]. *Guatteri and Spudich* [1998] give three possible factors that may lead to rake changes: (1) a low initial stress level (allowing an almost complete stress drop); (2) spatial variations in the direction of initial stress, and (3) slip in the direction of the current shear stress and not in the direction of initial shear stress during the propagation of the rupture. The two first conditions can be related. That is, low initial shear stress could result from a nearly fault-normal compression. In that case, small variations in the geometry and orientation of the fault (changes in dip angle as well as changes in strike) can lead to large variations in the direction of initial stress. In our model, the shear stress distribution is initially heterogeneous (see Figure 5, right) due to the previous slip history only and keeps evolving as the rupture propagates. Note that slip is forced to be in the direction of the current shear stress. We observe rake changes during the (quasi-static) propagation of an event on the (planar) strike-slip fault (Figure 7), in a mostly strike-slip regime with a small fault-normal component. We also observe a heterogeneous distribution of the static (final) rake. The average static stress drop is 11 MPa relative to the stress state at the initiation of the event (the maximum stress drop is on the order of 70 MPa but is reached only for two cells; see more details in section 3.4). This range of values is consistent with the ones obtained for the 1995 Kobe earthquake, for which *Bouchon et al.* [1998b] obtained 10 MPa and for the 1992 Landers earthquake, for which *Bouchon et al.* [1998a] obtained a maximum static stress drop of 20 MPa. The rake angle varies between 180° and 165°, with the maximum rake angle rotation at the edges of the upper half of the patch that slipped (*Spudich's* [1992] review mentions rotations from ±15° to ±50°). Finally, at the time this rupture initiates, the part of the fault that breaks may be considered weak ($\lambda \sim 0.45$), compared to the surrounding cells ($\lambda \sim 0.35$, e.g., reduced pore pressure from previous ruptures).

3.4. Fault Interaction: Separating the Effects of Shear Stress and Pore Pressure

Plate 1 shows the evolution of pore pressure (first column) and shear stress (second column) on the strike-slip fault (left) and on the dipping fault (right) during the same $M_w = 7.20$ event on the strike-slip fault described in section 3.3. Each subplot corresponds to cumulative changes of either pore pressure or shear stress (cumulative stress drop distributions) with respect to their state when the event initiated (not absolute values). Since the propagation is calculated in a quasi-static manner, we show snapshots of the pore pressure and shear stress state at different steps in the computer calcula-
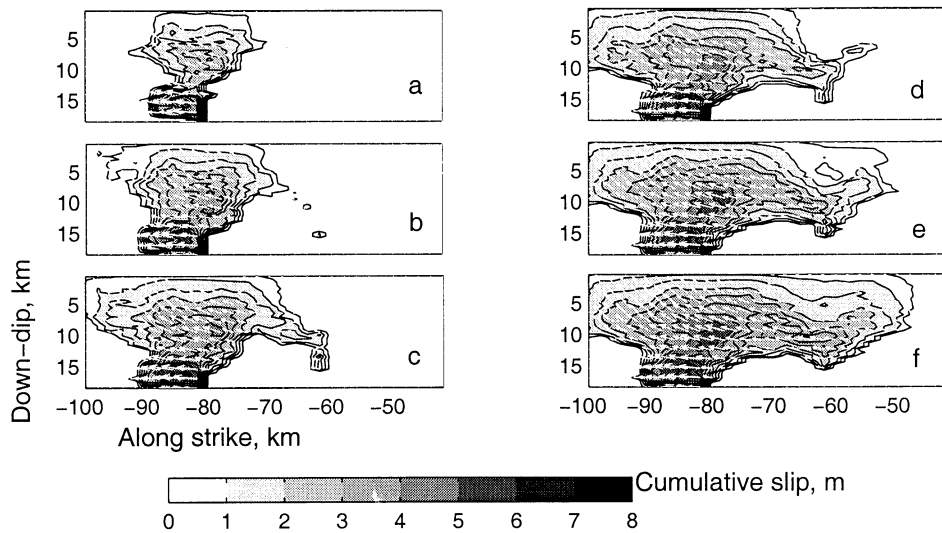
Figure 7. The propagation (a through f) of a large rupture ($M_w = 7.2$) occuring at t=5541.78 years on the strike-slip fault. The gray scale shows the cumulative slip, and the arrows show the change in the rake angle during the event (the updip component is shown with a vertical exageration of 10). Although the rupture initiates at x=-82 km, the rupture front "jumps" to x=-60 km and keeps on propagating. We can notice changes in the rake angle with rupture propagation. Note that the aspect ratio is not preserved.

tion for t=5541.78 years, and not at different "times." There were 194 cycles through the "rupture propagation" loop. The frames show row by row respectively the first, the twentieth, the sixtieth, the hundredth, the 193rd and the 194th (and last) iteration. Changes in pore pressure are due both to poroelasticity (and hence to the stress transfer during the rupture propagation) and to the redistribution of pore pressure itself.

On Plate 1a (top) we see that within the first cycle, only one cell failed on the strike-slip fault (secund column). The stress drop on this cell (-40 MPa) loads (through stress transfer) the other cells in the fault system. The first frame shows the poroelastic effect on the strike-slip fault due to the stress redistribution after this failure. ΔP_{f_1} is very small ($\pm 2 \times 10^{-5}$ MPa) compared to the same effect on the dipping fault shown on the third column ($\Delta P_{f_2} = \pm 2 \times 10^{-3}$ MPa). We also notice a small increase in shear stress (fourth column, $\Delta \tau_{f_1} = \pm 2 \times 10^{-5}$ MPa) 1 order of magnitude smaller than the change in pore pressure. Both changes on the dipping fault are located in the part of the fault closest to the strike-slip fault ($\approx$10 km) and are maximum at 12.25 km depth, centered on $x \approx$-82 km, like the strike-slip initial failure.

Plate 1b shows the state on the two faults after 20 iterations. The first frame shows the redistribution of pore pressure to the neighboring cells of the first failed cell. This plot is in full scale. The magnitude of the fluid pressure changes due to the opening of the seals is much larger than the poroelastic effect and mask it. As pointed out in section 2.2, this redistribution was enough to initiate failure in some of the surrounding

cells and the code cycles again in the stress transfer loop (second frame). The third frame shows the increase of the poroelastic effect ($\Delta P_{f_2} = \pm 0.1$ MPa) and the fourth frame shows the shear stress changes both from stress transfer from the strike-slip fault and from the two triggered failures on the dipping fault itself. Because the order of magnitude of the local stress transfer is much greater than the one of the interfault transfer, we chose to use a saturated scale on all the subplots of the right most column (except the first row). The absolute values of $\Delta \tau_{f_2}$ are in the range ± 2 MPa. The next three rows (Plates 1c, 1d and 1e) show the propagation of the strike-slip rupture and the newly triggered failures on the dipping fault. Plate 1f, corresponding to the last cycle, shows the final redistribution of stresses and pore pressure on both faults. In order to show the final poroelastic effect on the pore pressure state of the dipping fault, again, we used a saturated scale. The absolute values of ΔP_{f_2} are in the range ± 1 MPa.

Poroelasticity has a larger effect on the dipping fault than on the strike-slip fault itself (see changes in the color bar), and on both faults, pore pressure redistribution is much more efficient than poroelasticity in changing the effective normal stress. Changes in shear stress are due to the assumed stress drop and to the redistribution of stresses. Notice in Plate 1, third and fourth columns, that some small failures are triggered on the dipping fault by the one propagating on the strike-slip fault in regions of increased pore pressure and increased shear stress but not in regions of increased shear stress and decreased pore pressure. As these cells fail, the magnitude of pore pressure change is about double than
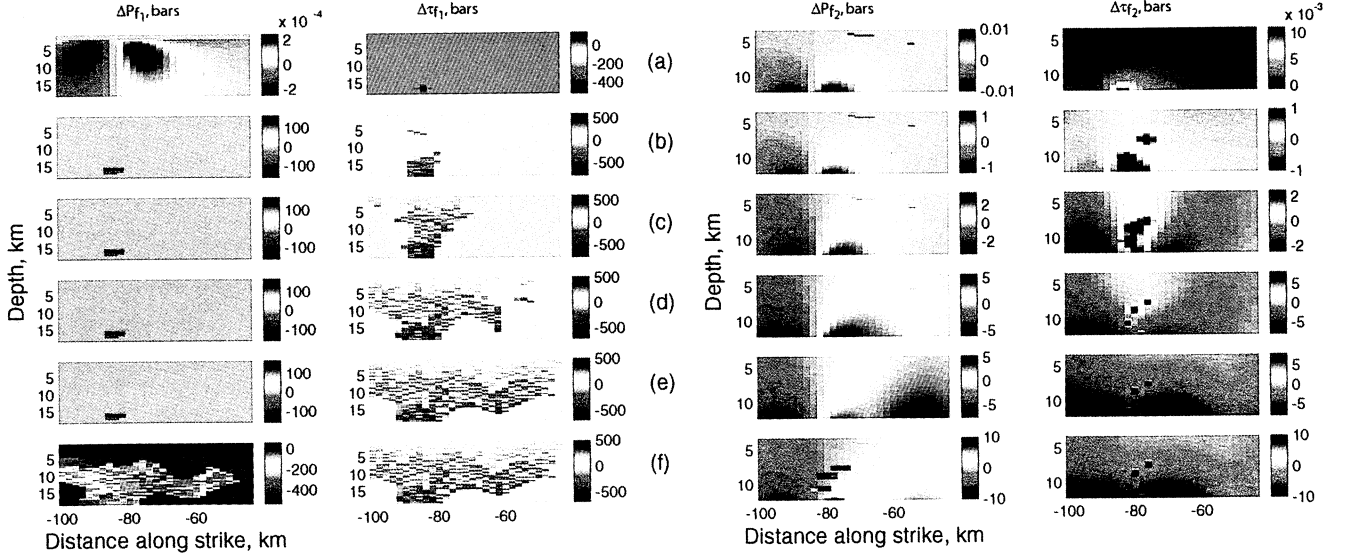
Plate 1. (a to f): Fault interaction. Pore pressure changes (first and third columns) and shear stress changes (second and fourth columns) on the strike-slip fault and on the dipping fault (respectively) during the $M_w = 7.2$ event on the strike-slip fault. Changes in pore pressure are due both to poroelasticity (and hence to stress transfer during the rupture propagation) and to the redistribution of pore presure itself. Changes in shear stress are due to the assumed stress drop and to the redistribution of stresses. Note different color bars for P_f for the two faults.

for shear stress at any cycle (1-0.5 for the twentieth cycle, 2-1 for the sixtieth, 5-3 for the hundredth, ...). The faults therefore interact, and in this example, a large event on the strike-slip fault triggered a $M_w = 5.00$ event on the dipping fault. Also notice that a large part of the dipping fault nearest the part of the strike-slip fault that ruptured is brought further from failure at the end of the event.

Table 2 demonstrates the efficiency of fault interaction: the coseismic triggering of seismicity on one fault due to the propagation of a rupture on the other fault. The time, the moment magnitude of the triggering event, and the moment magnitude of the triggered event on the receiver fault are given. We chose to show only the coupled triggering-triggered events including at least one event of moment magnitude M_w greater than 6.9. In all the cases but one the triggering events are large events ($6.9 < M_w < 7.8$) and the magnitude of the triggered events range from 4.03 to 5.97. The exception (in parentheses in Table 2) occurs at t=4585.5 years, when a $M_w = 5$ strike-slip event triggered a $M_w = 7.11$ on the dipping fault. Within the 9300 years of simulation, 63 earthquakes show $M_w > 6.9$ on the strike-slip fault. Only 30 of them trigger another earthquake coseismically. The proportion is the same for the dipping fault: 16 events with $M_w > 6.9$ among which only 7 related to an event on the strike-slip fault during the same time step. In principle, then, the strike-slip event could trigger a large event on the dipping fault (or vice versa) if the critical stress state on the receiver fault is sufficiently organized to support a spontaneous rup-

ture. In this simulation the largest triggered event is a $M_w = 5.97$, except a $M_w = 5.07$ event that started on the strike-slip fault triggered coseismically a $M_w = 7.11$ on the dipping fault (t=4585 years), see Table 2.

3.5. Total Local Stress Direct Calculation

The orientation and magnitude of the principal components of regional stress tensor are essential for understanding the physics of faulting, for evaluating the role of crustal fluids in the rupture process, and for seismic hazard assessment through the calculation of the optimal orientation of fault planes and expected tectonic regimes (ΔCFS [e.g., *Nalbant et al.*, 1998; *Stein et al.*, 1997]. However, as pointed out by *Zoback* [1992] and *Scholz* [2000], reliable direct in situ stress measurements [*Zoback and Healy*, 1992; *Townend and Zoback*, 2000] or evaluation (e.g., by inversion of focal mechanisms [*Hardebeck and Hauksson*, 1999]) are not straightforward. The regional stress is defined as a far-field tectonic load with respect to faults of interest. Accurate measurements are difficult because they should be made far from active faults to avoid fault-induced perturbations and also far from folds to avoid local perturbations of the regional stress. Because our model monitors the complete stress tensor in the whole fault system (on and off fault), we can calculate the principal stresses along any profile, at any depth, and for different times. We can therefore quantify stress partitioning (e.g., different tectonic regimes near the thrust fault compared to close to the strike-slip fault) and the rotation of the maximum

Table 2. Coseismic stress triggering between the two faults. M1 and M2 refer to the moment magnitude (M_w) of strike-slip fault and dipping fault events, respectively, and are calculated from the scalar seismic moment M_O via equation (6). The triggering event is always the larger of the two, except at t=4585.5 years, see row in parentheses.

Time (years)	Triggering Event	Triggered Event
2137.7	M1= 7.00	M2= 4.60
2873.7	M1= 7.10	M2= 4.75
3300.1	M2= 7.00	M1= 5.00
3622.8	M1= 7.10	M2= 5.10
3639.9	M1= 7.35	M2= 4.70
3870.4	M2= 7.00	M1= 4.35
4148.0	M1= 7.10	M2= 4.90
4252.5	M1= 6.95	M2= 5.35
4286.1	M1= 7.30	M2= 6.00
4560.6	M1= 7.11	M2= 5.15
(4585.5	M1= 5.10	M2= 7.10)
4618.0	M2= 7.45	M1= 5.75
4718.1	M1= 7.00	M2= 4.50
4939.7	M1= 7.00	M2= 4.80
5129.2	M1= 7.10	M2= 5.10
5225.3	M1= 7.10	M2= 4.50
5541.8	M1= 7.20	M2= 5.00
5601.1	M2= 7.00	M1= 4.05
5788.8	M1= 7.50	M2= 5.00
5801.4	M1= 6.90	M2= 4.90
5843.4	M1= 7.40	M2= 6.00
5908.0	M1= 7.00	M2= 4.30
5972.6	M1= 7.25	M2= 5.50
6012.8	M1= 7.05	M2= 5.10
6082.7	M1= 7.50	M2= 5.05
6190.9	M2= 6.90	M1= 4.10
6411.9	M1= 7.50	M2= 5.00
6613.9	M1= 7.10	M2= 4.90
6621.6	M1= 7.40	M2= 5.05
6773.6	M2= 7.10	M1= 5.00
6988.1	M1= 7.70	M2= 4.70
7929.7	M1= 7.20	M2= 4.60
8172.1	M1= 7.00	M2= 4.65
8476.8	M1= 7.60	M2= 4.20
8528.7	M1= 7.70	M2= 4.35
8786.4	M1= 7.15	M2= 4.30
8828.3	M1= 7.20	M2= 4.05

horizontal stress near the plate boundary and study its relation with the seismic slip recorded at that time during the simulation. In this preliminary study the "local" stress tensor was calculated on a horizontal grid at 8.5 km depth and at t=9300 years. The area that we investigate has the length of the faults and a width (y axis) about twice the depth of the dislocation plane on which the basal plate motion is applied. The strain tensor is computed as the superposition of displacements from plate motion and the cumulative slip displacement on the two faults in the geographical reference frame. We can determine the corresponding stress tensor through Hooke's law and then distribute the lithostatic stress calculated at the given depth to the isotropic part of the tensor. We then calculate the eigenvalues and eigenvec-

tors of the stress field. In the absence of slippage on the faults, at a given depth, the stress orientation shows a small gradual change from about $-48°$ near the plate boundary to a constant value about $-55°$ for $y \geq 35$ km (a distance from the plate boundary twice as large as the depth of the basal dislocation plane). This angle reflects the small normal component of the plate velocity vector (almost pure shear configuration, plus a small compressive component). The ratio $R = (\sigma_2 - \sigma_3)/(\sigma_1 - \sigma_3)$ is ~ 0.5, and σ_2 is vertical, corresponding to a strike-slip regime, with an optimal orientation for slip of about $-18°$.

Figure 8 shows the angle between the horizontal component of the maximum principal stress σ_1 and the strike of the faults, calculated after 9300 years of simulation, and including the cumulative fault slip. The directions of the three principal stresses are represented at several locations with arrows for the horizontal stresses and circles for the vertical ones. The orientation of σ_1 varies between $-65°$ (locally $-70°$) and $-35°$. The two extreme values are confined to small areas, whereas in most of the region the angle is in the range $[-45°, -58°]$. Other noticeable features include two regions where σ_3 is vertical, leading to a compressive plus strike-slip optimal tectonic regime. One of these zones extends roughly between -20 and 100 km along x and 25 and 35 km along y, and the other one, much smaller, lies at $x \geq 40$ km and $10 \leq y \leq 15$ km. They are just below and just above the dipping fault, respectively, in an x interval corresponding to the last large earthquake on the dipping fault. Just to illustrate how much an earthquake can rotate the surrounding stress field, we consider two examples. The $M_w = 7.2$ strike-slip event that was studied in the other sections induced rotations of σ_1 of $\pm3°$, whereas an earthquake of the same magnitude on the dipping fault (t=6246 years) induced rotations of $\pm5°$, for both cases, mostly in a region $y = \pm5$ km from the intersection of the fault with the horizontal plane.

Notice that our chosen fault system was not optimally oriented, so large slip deficit accumulated as long times were needed for the initial failure on the both faults (especially the dipping fault). The seismicity on the dipping fault could start only when the pore pressure was high enough to considerably reduce the Coulomb failure stress. By calculating R and knowing which principal stress is vertical, maps of the optimal tectonic regimes as well as a map of the corresponding planes (dip and strike) optimally oriented for failure in the country rock can be obtained. This result points to the necessity of generating new faults in response to the evolving stress field, and this is currently being developed.

3.6. Map and Cross Sections of ΔCFS and Comparison with Seismicity Distribution

Major simplifications of current stress transfer models are the assumptions (1) that the total slip from an earthquake can be averaged across a dislocation surface,
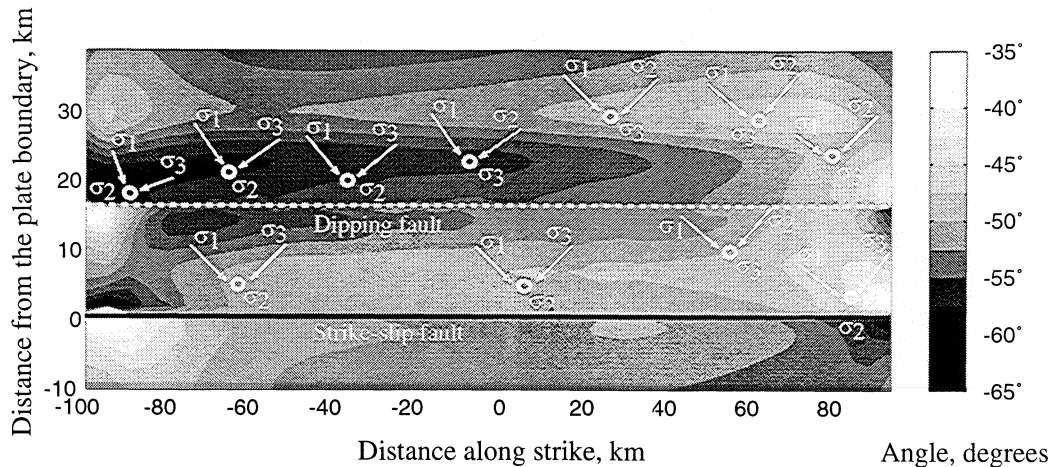
Figure 8. Local stress. Principal components are on a horizontal plane at 8.5 km depth for t=9300 years. The gray scale shows the angle of σ_1 with respect to the strike of the faults. The arrows show the directions of the principal stresses. Note that σ_2 is mostly vertical but that σ_3 can also be the vertical stress, denoting a transpressional regime.

and (2) the pore pressure state is homogeneous and its effect on the effective stress can be described through an apparent friction coefficient (μ'). The average slip is then used to calculate ΔCFS at a particular depth along faults of a prescribed orientation, typically vertical strike-slip faults. This simplification restricts the evaluation of along-strike changes in ΔCFS because the complex slip at depth is smoothed out. An alternative approach is to use seismic and geodetic techniques to evaluate more complex slip distributions, which can then be used as input to a stress transfer code. This approach is useful but requires extensive studies of a particular earthquake in a specified region, does not consider heterogeneous pore pressure distributions, and must always be "after the fact." The approach pursued here is to build a forward model that captures the dominant physics of the earthquake process, and then to use the model to evaluate spontaneous ruptures from a variety of fault geometries to systematically investigate the ΔCFS phenomenon, both on prescribed faults where pore pressure and stresses are monitored and on optimally oriented faults. In the latter case, the regional stress (orientation and magnitude of the principal stresses) is calculated directly from plate motion and the slip history of the fault system. We used the slip distribution in Figure 7 as input to a simple stress transfer code and show ΔCFS resolved on vertical optimally oriented faults as well as on the two prescribed faults of our model.

In the former case, we consider a simplified regional stress with σ_1 much larger than the two other components, with the magnitude and direction determined by the model at that time: 200 MPa, oriented -40° to the plate boundary. The stress difference (($\sigma_1 - \sigma_3$)/2) is between 50 and 100 MPa. These high values are, of course, unrealistic and demonstrate why future models must allow for the creation of new faults in response

to the regional stress field. The apparent friction coefficient μ' is chosen as 0.5. The calculation was performed for a depth of 8.5 km, and the intersection of the horizontal plane with the faults lies at y=0.7 km for the strike-slip and at y=15.5 km for the dipping fault. For the case of vertical planes, the optimal orientation (see lines on Plate 2) spans a small range of angles, from [-10.2,-6.3] degrees to the strike of the faults within ±5 km from the strike-slip fault to [-8.7,-8.2] (the "far-field" value, due only to the regional stress for $\mu' = 0.5$ is 8.3). These rotations are small because the calculated regional stress is much larger than the stress perturbation due to the earthquake (see Plate 1 and discussion by *King et al.* [1994]). As discussed in section 3.5, this high regional stress (a usual value in CFS studies is 100 bars) is due to the high strain energy stored in the country rock near the boundary, a direct consequence of both the choice of a uniform plate motion vector all over the basal dislocation ($\sim$40 km) and the orientation (nonoptimal) of the prescribed faults. On the optimally oriented vertical planes, ΔCFS was calculated and Plate 2 shows a large stress-released area, as well as two small areas that were brought closer to the failure. This pattern corresponds to that expected for right-lateral strike-slip events [*King et al.*, 1994].

Plate 3 shows the superposition of the change in coulomb failure stress with subsequent seismicity (next 20 years) on fault 1 (Plate 3a, top) and on fault 2 (Plate 3b, top), as well as the initial proximity to failure on the two faults at t=5541.78 years (Plates 3a and 3b, bottom). For these faults, ΔCFS was calculated using model results of shear stress, normal stress, and pore pressure, with a static friction coefficient of 0.6. On the strike-slip fault we note that all 15 events (magnitudes from 4.06 to 5.09) occurred in areas that were brought closer to failure (ΔCFS from +1 bar to +100 bars), which is consistent with the static stress trans-
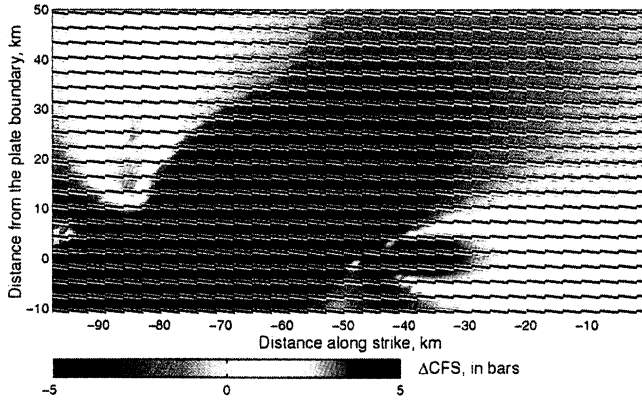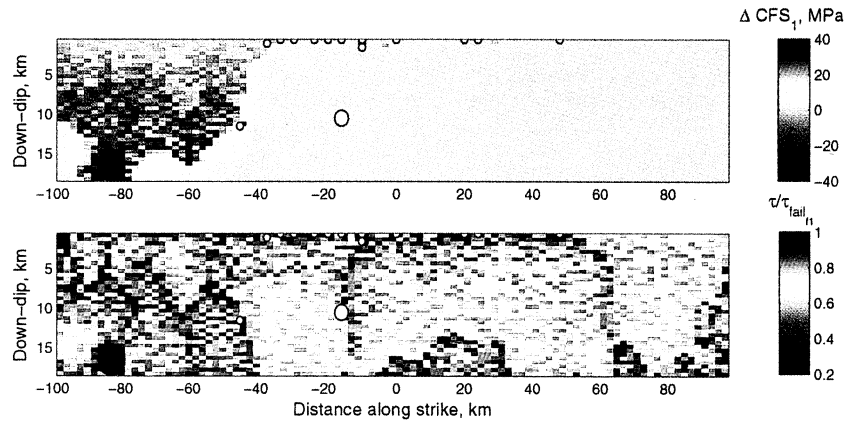
Plate 2. Static changes in Coulomb failure stress on optimally oriented vertical planes at 8.5 km depth after the same $M_w = 7.2$ event on the strike-slip fault: map view, with $\mu' = 0.5$, σ_1=200 MPa, oriented $-50°$ to the strike of the faults

fer approach. No events initiated in the zone of high positive ΔCFS between x=-40 and -20 km because the stress state on the strike-slip fault prior to the rupture was far from the Coulomb failure stress ($\tau/\tau_{\text{fail}} < 0.8$).

This corresponds to the stress drop due to a previous event, see Plate 3b. On the dipping fault the distribution of the 43 hypocenters does not look related to the ΔCFS pattern but to the areas that were already close to the failure before the triggering event. However, no earthquake occurred in the area of largest decrease in CFS, even if this area was very close to failure (Plate 3b, bottom, $\tau/\tau_{\text{fail}} \geq 0.8$) prior to the triggering event. In this case, the stress transfer from the first event induced a delay. Although the positive values of ΔCFS are rather small (commonly ¡1 bar), the number of earthquakes generated within the 20 years following the event is greater on the dipping fault than on the strike-slip fault. This is related to the difference in the stress state on the two faults at the initiation of the rupture at t=5541.78 years.

A direct comparison of the match between ΔCFS maps or cross sections and seismicity is now possible, allowing for a detailed investigation of the importance of a precise regional stress tensor and of an actual pore pressure distribution by opposition to an assumed apparent friction coefficient. The existence (or not) of a threshold value (i.e., above which an increase in CFS

(a) Strike-slip fault
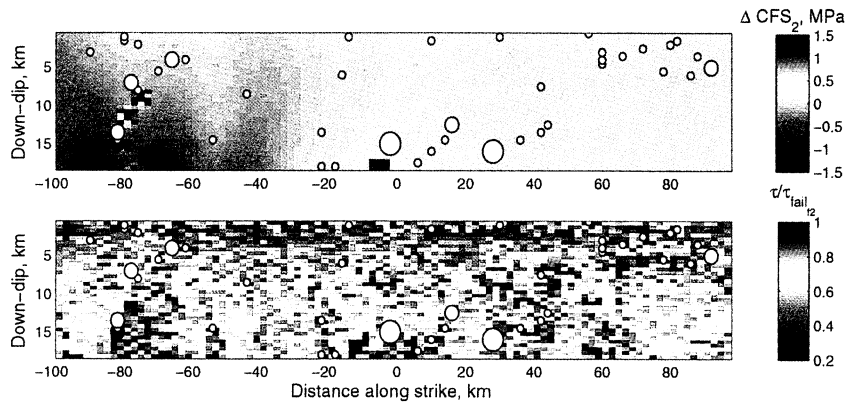
(b) Dipping fault

Plate 3. Static changes in Coulomb failure stress and initial proximity to failure (τ/τ_{fail}) (a) on the strike-slip fault, and (b) on the dipping fault, with hypocenter distribution for the next 20 years of simulated seismicity.

will promote seismicity whatever initial stress state is on the faults [*Ziv and Rubin*, 2000]) can also be investigated.

4. Discussion and Conclusions

4.1. Key Features of the Model

We have constructed a simple forward three-dimensional fault interaction model, driven by plate motion and pore pressure that includes dislocation theory, poroelasticity in undrained conditions, mechanisms for pore space reduction, small-scale coseismic changes in hydraulic properties, and frictional dilatation. We monitor the full stress tensor in any location in the elastic half-space and pore pressure on both faults. Reasonable assumptions are made about the initial heterogeneity. Cells which have a comparatively high pore pressure increase rate prove to be more often hypocenters. However, there is no direct link between this rate and the size of the events; that is, even if failures initiate more often in these cells, they propagate only if the surrounding cells are critically stressed. Preliminary results of this fully forward model show a complex evolutionary stress state in our fault system as well as a nonperiodic seismicity catalog that follows the GR law. Ruptures exhibit complex slip distributions, and the rake angle changes dynamically during the propagation of a rupture. Interaction between the faults is observed from coseismic shear stress changes as well as pore pressure changes on the dipping fault during large ruptures on the strike-slip fault. The result is small triggered events on the dipping fault. A simple static stress transfer model shows a good correlation between zones of positive change in Coulomb failure stress and subsequent hypocenter distribution, also showing the importance of the initial stress distribution on the induced seismicity.

4.2. Advantages of the Model

The model provides a general framework to study the behavior of large-scale transpressional and transtensional systems (such as the San Andreas fault; the North Anatolia fault, and the Dead Sea Transform). It can be used to study the stress state evolution to determine the relative contribution of plate motion loading and pore pressure changes, and spatiotemporal rotations of the principal axes of the "regional" stress tensor that combines plate motion, slip along faults, and the overburden.

The model can also be used as a tool to study conditions for rake angle changes during rupture on a fault. A thorough analysis of the influence of the fault geometry (e.g., local changes in dip angle), of the initial stress distribution, and of the regional stress (e.g., changes in the amount of normal stress) can be carried out.

The model can be used to study multiple fault interaction to determine some controlling factors. We show the competing poroelastic effect and shear stress transfer (Plate 1, third and fourth columns) can trig-

ger events only in zones of increase in shear stress and increase in pore pressure. The poroelastic increase in P_f is also larger than the change in shear stress by a factor of 2 in this example (when failures happen on the receiver fault). However, a study of the entire synthetic catalog is needed to discriminate between these two phenomena.

It is also interesting to note that pore pressures sometimes exceed the minimum principal stress at shallow depth during the pore pressure redistribution phase. This could induce some hydrofracture-related damage in, and normal to, the fault zone providing another complexity to the hydraulics of the system.

4.3. Limitations of the Model

The model can be used to investigate a wide range of phenomena. However, some important processes have not been addressed and need to be considered. First, diffusion processes are ignored. Using a simple one-dimensional diffusion equation (equation (7)):

$$\frac{\partial P_f}{\partial t} = \frac{k}{\eta\beta} \frac{\partial^2 P_f}{\partial x^2}, \qquad (7)$$

where k is the permeability, η is the viscosity and β is the total compressibility, we find that if $k_{rupture}$ is of the order of $10^{-15} m^2$ (for a viscosity about 1.9×10^{-4} Pa s and a maximum pressure gradient from lithostatic to hydrostatic), the time necessary to equilibrate fluid pressure over a cell size (km-scale) is of the order of, or less, than the average time step (days). Since fluid pressures are redistributed at the end of an event, the error due to the permeability switch is not significant. For larger events, pore pressures are redistributed each time stress equilibrium is reached, but this redistribution may induce a subsequent propagation of the event. In this case, pore pressures should not be redistributed instantaneously, especially over large patches. A more realistic model should include pore pressure diffusion and not redistribution.

Second, frictional heating and the subsequent increase in pore pressure probably play an important role in fault zones and will be introduced into the model. *Lachenbruch and Sass* [1980], *Mase and Smith* [1985] and *Spray* [1995] show that temperatures can reach 1000°C during high-speed slip experiments performed on Westerly granite. Such large temperature changes can expand pore fluids, can initiate melting and dehydration reactions, and can provide a mechanism for afterslip. Presumably, the frictional heating is not generated uniformly over the fault surface but is more likely to be localized at asperity contacts, which may provide an additional source of complexity along the faults. An interseismic temperature depth profile should also be introduced because of the influence of temperature on the kinetics of geochemical reactions and hence on the fluid content [*Quattrocchi*, 1999]. The latter modification might also be efficiently coupled to a more realistic $\dot{\Gamma}$ in the source term. A full study of heat transfer in a

saturated porous medium should take into account the rate of conductive heat transport, the rate of convective transport, the rate of heating due to the reversible work done on the fluid, the rate of frictional heating, and the rate of internal heat storage for the solid-fluid composite [*Mase and Smith*, 1985]. This can be solved numerically but introduces many unconstrained parameters. Our general model framework can be used to investigate these processes but it is beyond the scope of the current work.

Third, all events in the model are "seismic", meaning that we implicitly assume unstable sliding at the onset of failure. *Segall and Rice* [1995] showed that high pore pressures affect the stability of sliding, and such a criterion should be considered in future models. This stability criterion [*Segall and Rice*, 1995] depends on the elastic properties of the surrounding country rock and on the pore pressures in the fault zone. Sliding stability affects the rate of stress accumulation on the faults, and at a microscopic scale, it induces compaction as already discussed [*Sleep and Blanpied*, 1994]. Finally, a uniform plate motion, even near the plate boundary, is a rough approximation that leads to high depth-dependent stress concentrations near the boundary.

4.4. Conclusion and Future Perspectives

This simple coupled system (i.e., a dipping fault and a subvertical strike-slip fault, in a transpressional environment) was chosen as a starting point because there are such examples in nature and because it was a way to investigate a fully three-dimensional fault system, including fault interaction, stress triggering and local stress field time evolution. This a priori choice of geometry allowed us to draw several conclusions. The most important is that it is essential for any forward model to include the dynamic generation of new faults in response to the evolving stress field, e.g., the initial nonoptimal orientation of the faults leads to a high strain energy in the system, an overpressured dipping fault, a high slip deficit and high maximum principal stresses in the surrounding country rock. The nonoptimal orientation of our system thus limits the generalization we can make. Nevertheless, we were able to show seismicity statistics in conformity with both theoretical and data-based results, realistic rupture propagation patterns, including changes in the rake angle, as well as the critical influence of fault zone fluids on the triggering of earthquakes from one fault to the other, via poroelastic effects (see section 3.4 as well as the self-organization of the stress state of the faults [*Miller et al.*, 1999]. Future work will include two main aspects: the model development toward the evolution of fault systems following the evolution of the principal stresses (dynamical fault generation), and a closer analysis of the "source terms" (fluid sources, compaction, damages, hydrofractures). Our long-term aim is to point to measurable properties (e.g., pore pressures, hydrofrac-

tures, seismicity catalogs of the area) in or around (e.g., stress orientation, surface strain, triggering) fault zones, which may allow inferences on the stress state of a given fault system.

References

Bak, P., and C. Tang, Earthquakes as a self-organized critical phenomenon, *J. Geophys. Res.*, 15,635–15,637, 1989.

Beeler, N., R. Simpson, S. Hickman, , and D. Lockner, Pore fluid pressure, apparent friction, and Coulomb failure, *J. Geophys. Res.*, 25,533–25,542, 2000.

Ben-Zion, Y., and J. R. Rice, Earthquake failure sequences along a cellular fault zone in a three-dimensional elastic solid containing asperity and nonasperity regions, *J. Geophys. Res.*, 14,109–14,131, 1993.

Ben-Zion, Y., and J. R. Rice, Slip patterns and earthquake populations along different classes of faults in elastic solids, *J. Geophys. Res.*, 12,959–12,983, 1995.

Blanpied, M. L., T. E. Tullis, , and J. D. Weeks, Effects of slip, slip rate, and shear heating on the friction of granite, *J. Geophys. Res.*, 489–511, 1998.

Bouchon, M., M. Campillo, , and F. Cotton, Stress field associated with the rupture of the 1992 Landers, California, earthquake and its implications concerning the fault strength at the onset of the earthquake, *J. Geophys. Res.*, 21,091–21,097, 1998a.

Bouchon, M., H. Sekiguchi, K. Irikura, , and T. Iwata, Some characteristics of the stress field of the 1995 Hyogo-Ken Nanbu (Kobe) earthquake, *J. Geophys. Res.*, 24,271–24,282, 1998b.

Byerlee, J., Model for episodic flow of high-pressure water in fault zones before earthquakes, *Geology*, 303–306, 1993.

Chester, F. M., J. P. Evans, , and R. L. Biegel, Internal structure and weakening mechanisms of the San Andreas fault, *J. Geophys. Res.*, 771–786, 1993.

Dascalu, C., I. Ionescu, , and M Campillo, Fault finiteness and initiation of dynamic shear instability, *Earth Planet. Sci. Lett.*, 163–176, 2000.

Dieterich, J. H., Modeling of rock friction -1. Experimental results and constitutive equations, *J. Geophys. Res.*, 2161–2168, 1979.

Ekström, G., R. S. Stein, J. P. Eaton, , and D. Eberhart-Phillips, Seismicity and geometry of a 110-km-long blind thrust fault 1. The 1985 Kettleman Hills, California, earthquake, *J. Geophys. Res.*, 4843–4864, 1992.

Gomberg, J., N. Beeler, , and M. L. Blanpied, On rate-state and Coulomb failure models, *J. Geophys. Res.*, 7857–7871, 2000.

Guatteri, M., and P. Spudich, Coseismic temporal changes of slip direction: The effect of absolute stress on dynamic rupture, *Bull. Seismol. Soc. Am.*, 777–789, 1998.

Hardebeck, J. L., and E. Hauksson, Role of fluids in faulting inferred from stress field signatures, *Science*, 236–239, 1999.

Harris, R. A., and S. M. Day, Dynamic 3d simulations of earthquakes on en echelon faults, *Geophys. Res. Lett.*, 2089–2092, 1999.

Hubbert, M. K., and W. W. Rubey, Role of fluid pressure in mechanics of overthrust faulting, *Bull. Geol. Soc. Am.*, 115–166, 1959.

Kame, N., and T. Yamashita, A new light on arresting mechanism of dynamic earthquake faulting, *Geophys. Res. Lett.*, 1997–2000, 1999.

King, G. C. P., R. S. Stein, , and J. Lin, Static stress changes and the triggering of earthquakes, *Bull. Seismol. Soc. Am.*, 935–953, 1994.

Lachenbruch, A. H., and J. H. Sass, Heat flow and energetics of the San Andreas fault zone, *J. Geophys. Res.*, 6185–6222, 1980.

Lockner, D. A., and J. D. Byerlee, How geometrical constraints contribute to the weakness of mature faults, *Nature*, 250–252, 1993.

Marone, C., The effect of loading rate on static friction and the rate of fault healing during the earthquake cycle, *Nature*, 69–72, 1998.

Mase, C. W., and L. Smith, Pore-fluid pressures and frictional heating on a fault surface, *Pure Appl. Geoph.*, 583–607, 1985.

Massonnet, D., M. Rossi, C. Carmona, F. Adragna, G. Peltzer, K. Feigl, , and T. Rabaute, The displacement field of the Landers earthquake mapped by radar interferometry, *Nature*, 138–142, 1993.

Meghraoui, M., T. Camelbeeck, K. Vanneste, M. Brondeel, , and D. Jongmans, Active faulting and paleoseismology along the Bree fault, lower Rhine graben, Belgium, *J. Geophys. Res.*, 13,809–13,841, 2000.

Miller, S. A., Y. Ben-Zion, , and J.-P. Burg, A three dimensional fluid-controlled earthquake model: Behavior and implications, *J. Geophys. Res.*, 10,621–10,638, 1999.

Miller, S. A., and A. Nur, Permeability as a toggle switch in fluid-controlled crustal processes, *Earth Planet. Sci. Lett.*, 133–146, 2000.

Miller, S. A., A. Nur, , and D. L. Olgaard, Earthquakes as a coupled shear stress-high pore pressure dynamical system, *Geophys. Res. Lett.*, 197–200, 1996.

Nalbant, S. S., A. Hubert, , and G. C. P. King, Stress coupling between earthquakes in northwest Turkey and the north Aegean Sea, *J. Geophys. Res.*, 24,469–24,486, 1998.

Nur, A., and J. D. Byerlee, An exact effective stress law for elastic deformation of rock with fluids, *J. Geophys. Res.*, 6414–6419, 1971.

Okada, Y., Surface deformation due to shear and tensile faults in a half-space, *Bull. Seismol. Soc. Am.*, 1135–1154, 1985.

Okada, Y., Internal deformation due to shear and tensile faults in a half space, *Bull. Seismol. Soc. Am.*, 1018–1040, 1992.

Pacheco, J. F., C. H. Scholz, , and L. R. Sykes, Changes in frequency-size relationship from small to large earthquakes, *Nature*, 71–73, 1992.

Pantosti, D., D. P. Schwartz, , and G. Valensise, Paleoseismology along the 1980 surface rupture of the Irpinia fault: Implications for earthquake recurrence in the southern Apennines, Italy, *J. Geophys. Res.*, 6561–6577, 1993.

Perfettini, H., R. S. Stein, R. W. Simpson, , and M. Cocco, Stress transfer by the 1988-1989 M=5.3 and 5.4 Lake Elsman foreshocks to the Loma Prieta fault: Unclamping at the site of peak mainshock slip, *J. Geophys. Res.*, 20,169–20,182, 1999.

Quattrocchi, F., In search of evidence of deep fluid discharges and pore pressure evolution in the crust to explain the seismicity style of the Umbria-Marche 1997-1998 seismic sequence (central Italy), *Ann. Geofis.*, 609–636, 1999.

Rice, J. R., Spatio-temporal complexity of slip on a fault, *J. Geophys. Res.*, 9885–9907, 1993.

Rice, J. R., Fault stress states, pore pressure distributions, and the weakness of the San Andreas fault, in *Fault Mechanics and Transport Properties of Rocks, Int. Geophys. Ser.*, vol.51, edited by B. Evans and T.-f. Wong, pp. 9885–9907, Academic, San Diego, Calif., 1992.

Rice, J. R., and M. P. Cleary, Some basic stress diffusion solutions for fluid-saturated elastic porous media with compressible constituents, *Rev. Geophys. Space Phys*, 227–241, 1976.

Robert, F., and A.-M. Boullier, Mesothermal gold-quartz veins and earthquakes, in *The Mechanical Involvement of Fluids in Faulting*, pp. 18–30, U.S. Geol. Surv., Reston, Va., 1993.

Robinson, R., and R. Benites, Synthetic seismicity models of multiple interacting faults, *J. Geophys. Res.*, 18,229–18,328, 1995.

Robinson, R., and R. Benites, Synthetic seismicity models for the wellington region, new zealand: implications for the temporal distribution of large events, *J. Geophys. Res.*, 27,833–27,844, 1996.

Rudnicki, J. W., Effect of pore fluid diffusion on deformation and failure of rock, in *Mechanics of Geomaterials*, edited by Z. Bazant, pp. 315–346, John Wiley, New York, 1985.

Rundle, J. B., A physical model for earthquakes, 1, Fluctuations and interactions, *J. Geophys. Res.*, 6237–6254, 1988.

Rundle, J. B., Derivation of the complete Gutenberg-Richter magnitude-frequency relation using the principle of scale invariance, *J. Geophys. Res.*, 12,337–12,342, 1989.

Scholz, C. H. The Mechanics of Earthquakes and Faulting. Cambridge Univ. Press, New York, 1990.

Scholz, C. H., Earthquakes and friction laws, *Nature*, 37–42, 1998.

Scholz, C. H., Evidence for a strong San Andreas fault, *Geology*, 163–166, 2000.

Segall, P., and J. R. Rice, Dilatancy, compaction, and slip instability of a fluid-infiltrated fault, *J. Geophys. Res.*, 22,155–22,171, 1995.

Sibson, R. H., Interaction between temperature and pore fluid pressure during an earthquake faulting and a mechanism for partial or total stress relief, *Nature*, 66–68, 1973.

Sibson, R. H., Fault-valve behavior and the hydrostatic-lithostatic fluid pressure interface, *Earth-Science Reviews*, 141–144, 1992.

Sibson, R. H., Geological evidence of fluid involvement in the rupture processes of crustal earthquakes, in, *The Mechanical Involvement of Fluids in Faulting*, pp. 31–38, U.S. Geol. Surv., Reston, Va., 1993.

Sleep, N., Ductile creep, compaction and rate and state

dependent friction within major fault zones, *J. Geophys. Res.*, 13,065–13,080, 1995.

Sleep, N., and M. L. Blanpied, Creep, compaction and the weak rheology of major faults, *Nature*, 687–692, 1992.

Sleep, N., and M. L. Blanpied, Ductile creep and compaction: A mechanism for transiently increasing fluid pressure in mostly sealed faults zones, *Pure Appl. Geoph.*, 9–40, 1994.

Spray, J. G., Pseudotachylyte controversy: Fact or friction?, *Geology*, 1119–1122, 1995.

Spudich, P. K. P., On the inference of absolute stress levels from seismic radiation, *Tectonophysics*, 99–106, 1992.

Stein, R. S., A. A. Barka, , and J. H. Dieterich, Progressive failure on the North Anatolian fault since 1939 by earthquake stress triggering, *Geophys. J. Int.*, 594–604, 1997.

Streit, J. E., and S. F. Cox, Asperity interactions during creep of simulated faults at hydrothermal conditions, *Geology*, 231–234, 2000.

Talwani, P., J. S. Cobb, , and M. F. Schaeffer, In situ measurements of hydraulic properties of a shear zone in northwestern South Carolina, *J. Geophys. Res.*, 14,993–15,003, 1999.

Townend, J., and M. D. Zoback, How faulting keep the crust strong, *Geology*, 399–402, 2000.

Voisin, C., M. Campillo, I. Ionescu, F. Cotton, , and O. Scotti, Dynamic versus static stress triggering and

friction parameters: Inferences from the November 23, 1980, Irpinia earthquake, *J. Geophys. Res.*, 21,647–21,659, 2000.

Yamashita, T., Simulation of seismicity due to fluid migration in a fault zone, *Geophys. J. Int.*, 674–686, 1998.

Yamashita, T., Pore creation due to fault slip in a fluid-permeated fault zone and its effect on seismicity: Generation mechanism of earthquake swarms, *Pure Appl. Geoph.*, 625–647, 1999.

Ziv, A., and A. M. Rubin, Static stress transfer and earthquake triggering: No lower threshold in sight?, *J. Geophys. Res.*, 13,631–13,642, 2000.

Zoback, M. D., and J. H. Healy, In situ stress measurements to 3.5 km depth in the Cajon Pass scientific research borehole: Implications for the mechanics of crustal faulting, *J. Geophys. Res.*, 5039–5057, 1992.

Zoback, M. L., First- and second order patterns of stress in the lithosphere": The World Stress Map Project, *J. Geophys. Res.*, 11,703–11,728, 1992.

D. D. Fitzenz and S. A. Miller, Department of Earth Sciences, Swiss Federal Institute of Technology, CH-8093 Zürich, Switzerland (fitzenz@erdw.ethz.ch)